Energy & Environmental Science

ROYAL SOCIETY OF CHEMISTRY

PAPER

View Article Online
View Journal | View Issue

Cite this: *Energy Environ. Sci.*, 2026, **19**, 2988

Beyond rapid nucleation: unveiling the role of solvent–precursor interactions in antisolvent-free perovskite fabrication

Yunfan Wang,†[a] Weiren Zhao, †[b] Juncheng Wang,†[c] Zhuoqiong Zhang, †*[d] Ziyao Yue,[a] Yuxuan Zhang,[a] Yiting Jiang,[e] Zixin Zeng, [a] Jie Zeng,[a] Hainam Do, [f] Hong Lu,[fg] Yuanhang Cheng,*[h] Johnny C. Ho, [a] Tom Wu, [d] Hin Lap Yip, [ae] Dewei Zhao *[c] and Sai-Wing Tsang *[ai]

Solution-processed antisolvent-free perovskites (AFPs) are promising candidates for scalable photovoltaic (PV) production. However, achieving high-quality AFP films typically requires stringent processing conditions, limiting reliability in large-scale manufacturing. Here, we employ machine learning (ML) to identify solvent additives that modulate the ambient temperature (T_A) processing window. This approach successfully reveals an additive that enables a record-wide T_A window, from 16 °C to 28 °C, with constantly high power conversion efficiencies (PCEs) exceeding 24%. Mechanistically, in contrast to the previously reported solvent-lead iodide (PbI_2) interaction model, we demonstrate that anchoring formamidinium (FA) cations with the additive to form stable adducts is essential. This interaction effectively suppresses crystallization kinetics, facilitating uniform precursor distribution and high-quality film formation. Importantly, these results challenge the conventional crystallization paradigm for solution-processed perovskites, which emphasizes rapid and complete nucleation during the initial stage of film deposition. Instead, we find that a uniform distribution of precursor ions, even without any nucleation, is sufficient to achieve high-quality perovskite thin films. This work not only demonstrates an effective ML-guided solvent selection strategy but also provides fundamental insight into the primary crystallization requirements for scalable production of high-quality perovskite PV thin films.

Received 9th January 2026,
Accepted 30th March 2026

DOI: 10.1039/d6ee00170j

rsc.li/ees

Broader context

Recently, solution-processed antisolvent-free perovskites (AFPs) have become promising candidates for scalable photovoltaic manufacturing. However, high-quality AFP films are still suffering from the stringent control of ambient temperature (T_A), typically constrained below 20 °C during solution deposition, which hinders large-scale reproducibility. Here, we employ a machine learning-guided strategy that replaces conventional trial-and-error approaches to identify solvents that significantly broaden the T_A processing window, from 16 °C to 28 °C, while achieving champion power conversion efficiencies (PCEs) exceeding 24% and maintaining at least 90% of this PCE across the entire T_A range. In addition, our findings reveal that the uniform precursor distribution enabled by solvent-based adducts is more critical for AFP fabrication than the traditionally emphasized rapid and complete perovskite nucleation. More importantly, a key prerequisite for forming such stable adducts has often been previously overlooked. In addition to stabilizing metal–halide–solvent adducts, it is also essential to stabilize the cations, thereby preventing competing reactions that can lead to non-uniform crystal growth.

[a] *Department of Materials Science and Engineering, City University of Hong Kong, Hong Kong SAR, 999077, P. R. China. E-mail: saitsang@cityu.edu.hk*
[b] *Bioinformatics Center, Institute for Chemical Research, Kyoto University, Kyoto, Japan*
[c] *College of Materials Science and Engineering & Institute of New Energy and Low-Carbon Technology & Engineering Research Center of Alternative Energy Materials and Devices, Ministry of Education, Sichuan University, Chengdu, China. E-mail: dewei_zhao@hotmail.com*
[d] *Department of Applied Physics, The Hong Kong Polytechnic University, Hong Kong SAR, 999077, P. R. China. E-mail: 18481965@life.hkbu.edu.hk*
[e] *School of Energy and Environment, City University of Hong Kong, Hong Kong SAR, 999077, P. R. China*
[f] *Department of Chemical and Environmental Engineering, University of Nottingham Ningbo China, Ningbo, 315100, China*
[g] *Perovskite Research Institute, Yangzhou Precision Systems Inc., Yangzhou, 225000, China*
[h] *School of New Energy, Nanjing University of Science and Technology, Jiangyin, Jiangsu, 21443, China. E-mail: yhcheng@njust.edu.cn*
[i] *Center of Super-Diamond and Advanced Films (COSDAF), and Hong Kong Institute for Clean Energy, City University of Hong Kong, Hong Kong SAR, 999077, P. R. China*
† These authors contributed equally: Yunfan Wang, Weiren Zhao, Juncheng Wang, and Zhuoqiong Zhang.

Introduction

Due to the remarkable optoelectronic properties of perovskites, PSCs have achieved a rapid increase in power conversion efficiency (PCE) from 3.8% to 27.0% and are regarded as a leading candidate for next-generation photovoltaics.[1–11] Among various fabrication approaches, solution-processed methods have garnered significant attention due to their simplicity, low cost, and scalability.[12,13] In particular, the antisolvent-assisted one-step method has been a popular technique for fabricating high-efficiency PSCs in laboratory settings, as it can effectively accelerate nucleation to improve film morphology.[2,14,15] However, this method is typically applied to small-area samples. For larger-area samples (>100 cm^2), variations in solvent extraction efficiency caused by differing degrees of antisolvent contact in different regions can result in non-uniform nucleation rates across the film, compromising film quality and hindering large-scale manufacturing.[9,16–18] Consequently, the development of antisolvent-free fabrication strategies has become an urgent priority.

In antisolvent-free fabrication, the absence of antisolvent extraction significantly retards nucleation, leaving a non-uniform distribution of some perovskite nuclei and a large amount of precursor ions after film deposition. While the ions diffuse toward existing nuclei to promote crystal growth, certain regions become solute-depleted, which in turn suppresses additional nucleation and leads to incomplete film coverage and pinholes.[19] This inherent competition between nucleation and crystal growth presents challenges in achieving uniform and high-quality perovskite films. To address this, Bu *et al.* introduced a solvent engineering strategy by adding *N*-methyl-2-pyrrolidone (NMP) into the formamidinium (FA)–cesium (Cs) lead triiodide precursor to form a PbI_2–NMP adduct in the deposited film.[20] This intermediate suppressed nucleation and crystal growth by preventing PbI_2 from directly reacting with FAI. The perovskite nucleation and crystal growth are initiated during the subsequent thermal annealing process. Different from the antisolvent approach, the authors demonstrated that a high-quality antisolvent-free perovskite (AFP) film can be achieved by a "two-step" method: a solvent-based intermediate is first formed in the deposited film, which is then followed by its *in situ* conversion to the perovskite phase through reaction with FA during the annealing process. Using this approach, the authors achieved high-efficiency AFP solar cells (AFPSCs) with a small-area PCE of 23.35% and a 17.1 cm^2 solar module with a PCE of 20.42%. Consequently, several attempts have been demonstrated using a similar approach to enhance the quality of AFP films.[21–23] Despite the success in producing high-quality AFP films and promising photovoltaic devices, it is questionable whether the formation of PbI_2–NMP adducts alone, as proposed by Bu *et al.*, is sufficient to suppress the crystallization kinetics. It is because FA^+ cations generally have a stronger interaction with the solvent and other precursor materials; the addition of FA^+ in the precursor solution will accelerate the nucleation.

Additionally, a significant challenge remains in antisolvent-free PSCs (AFPSCs) due to their high sensitivity to ambient temperature (T_A). The reported high-efficiency AFPSCs are typically fabricated at a T_A below 18 °C to ensure optimal crystal and film quality.[21,24] However, for industrial-scale applications, the cooling process increases production costs and reduces competitiveness in the photovoltaic market. Moreover, restricting the fabrication process to a narrow T_A range complicates production control and negatively impacts the product yield in scalable manufacturing. Previous studies have shown that T_A significantly influences crystallization dynamics, and therefore the film quality, in antisolvent-assisted perovskites. Although crystallization can be regulated *via* solvent engineering to control the ion coordination,[25–28] a conventional trial-and-error solvent selection approach is time-consuming and inefficient, necessitating new methodologies for systematic optimization. Recently, machine learning (ML) has offered a promising solution to this challenge. With its ability to analyze large datasets and uncover complex correlations, ML has become a powerful tool in materials science, enabling efficient screening of candidates and minimizing experimental efforts.[29,30] Recently, several attempts to employ ML in perovskites have demonstrated success in identifying new passivation molecules and interlayer materials to enhance the PSC lifetime and PCE.[31,32] These promising results underscore the utility of ML in addressing persistent challenges in perovskite photovoltaics, offering a pathway to accelerate the commercialization of the technology.

In this work, we report an ML-guided solvent engineering strategy to regulate the nucleation kinetics in FA-based AFPs ($FA_{0.92}Cs_{0.08}PbI_3$), enabling the fabrication of high-performance AFPSCs over a wide T_A processing window. A database of several hundred solvents was preprocessed and clustered into groups based on a set of physicochemical descriptors. A cluster containing solvents that have previously been employed in AFP was selected for experimental validation and model training. Using this ML-guided strategy, we successfully achieved consistently high-efficiency AFPSCs with a PCE over 24% in a broad T_A processing window from 16 °C to room temperature (24 °C). The developed recipe also demonstrated promising scalability, and a slot-die-coated AFP module with a large aperture area of 693 cm^2 achieved a PCE of 17.6%. In addition, density functional theory (DFT) calculations and *in situ* characterization studies were conducted to further elucidate the mechanism underlying the performance enhancement of the devices induced by the ML-selected solvents. Our findings reveal that the uniform precursor distribution enabled by solvent-based adducts is more critical for AFP fabrication than the traditionally emphasized rapid and complete perovskite nucleation. More importantly, a key prerequisite for forming such stable adducts has often been previously overlooked. In addition to stabilizing metal–halide–solvent adducts, it is also essential to stabilize the cations, thereby preventing competing reactions that can lead to non-uniform crystal growth. Overall, the ML-assisted strategy bridges computational exploration with hypothesis-driven experiments, offering a synergistic pathway that accelerates solvent discovery while deepening the understanding of solvent–solute interactions during perovskite crystallization.

Results and discussion

Widening the T_A window based on an ML-guided solvent engineering strategy

Solvent engineering is a critical strategy for regulating the crystallization process of perovskite films to improve their quality. However, traditional solvent selection often relies on experience and trial-and-error methods, which are time-consuming and inefficient. In this work, we proposed an integrated workflow (Fig. S1, SI) that combines ML with experimental validation to accelerate the identification of optimal solvents within a defined chemical space. Firstly, we constructed a dataset of 348 solvents characterized by 168 physicochemical descriptors (Fig. S2, SI). Using an algorithmic clustering approach, the dataset was organized into 23 clusters based on physicochemical properties (Fig. S3–S6, SI). For example, NMP (#13), a commonly used solvent additive in AFP fabrication, is assigned to the 17th cluster, as shown in Fig. 1a. Since solvents within the same cluster are expected to exhibit similar structural and physicochemical properties, we hypothesized that other solvents in this cluster could also serve as promising candidates. Guided by this classification, we can experimentally validate these solvents to assess

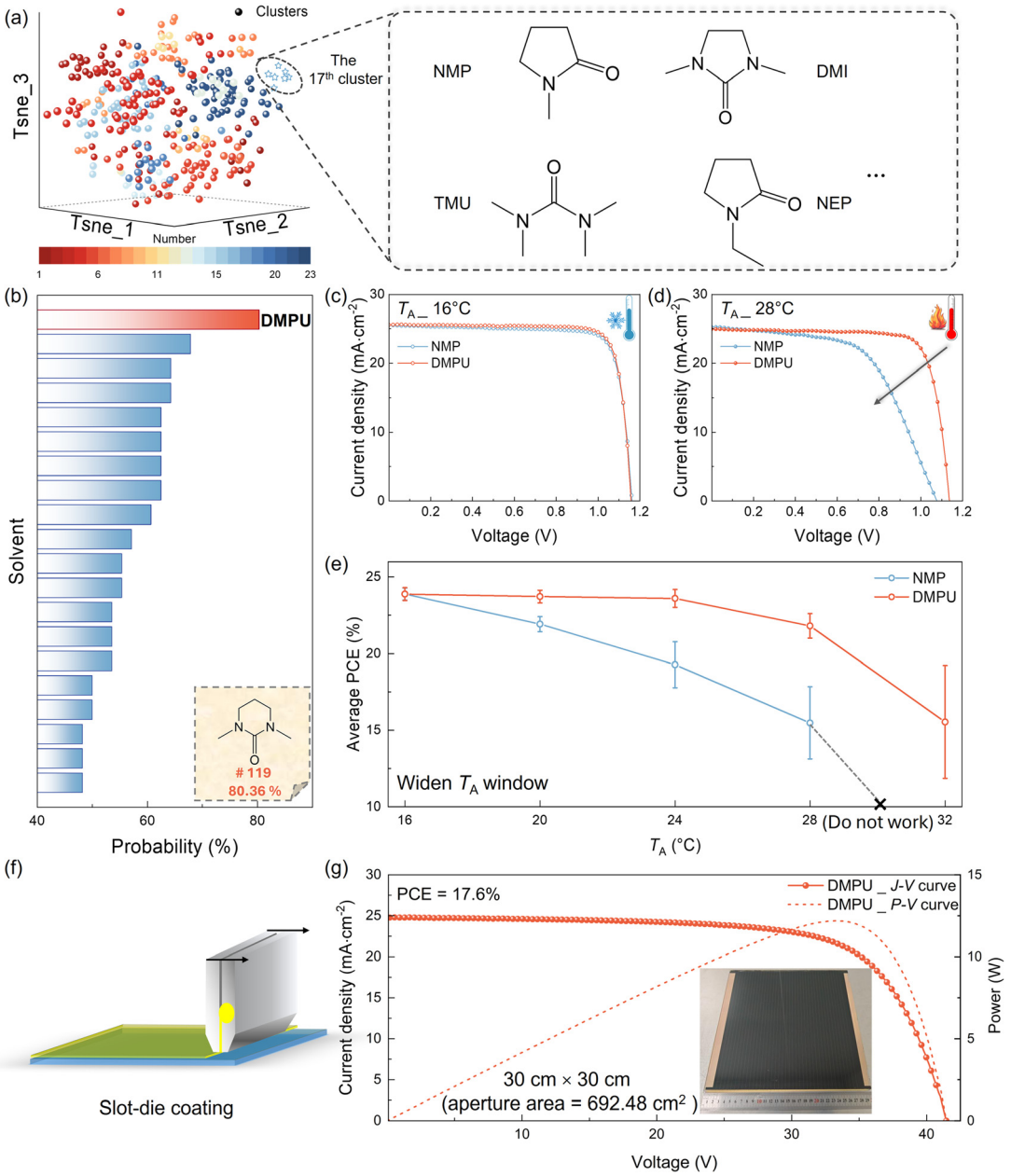

Fig. 1 Widening the T_A window based on an ML-guided solvent engineering strategy. (a) Molecular structure of grouped solvents in the 17th cluster. (b) Top 20 solvents identified by the ensemble model. The *J*–*V* curves of different solvent-treated AFPSCs fabricated at T_A values of (c) 16 °C and (d) 28 °C. (e) PCE statistics of different solvent-treated AFPSCs fabricated under different T_A conditions. (f) Schematic drawing of slot-die coating for large area solar module fabrication. (g) *J*–*V* and *P*–*V* curves of DMPU-treated solar module fabricated at a T_A of 20 °C.

their suitability. In contrast, dimethyl sulfoxide (DMSO _ #57), a widely used solvent additive in the antisolvent-assisted perovskite approach, is grouped into a different cluster. To verify the reliability of this grouping, we also performed experimental validation on DMSO. The corresponding morphological and optoelectronic properties demonstrate that the DMSO-treated film is entirely unsuitable for AFP fabrication due to poor surface coverage and uneven grain distribution (SI, Fig. S8). In contrast, most solvents in the 17th cluster are well-suited for AFP fabrication, effectively suppressing pinhole formation even at higher T_A, such as tetramethylurea (TMU _ #2) and 1,3-dimethyl-2-imidazolidinone (DMI _ #120) (SI, Fig. S9–S11). However, variations in solvent performance are still observed within the same cluster. For instance, TMU-treated films exhibit superior morphology even at a high processing T_A of 28 °C, whereas films treated with *N*-ethylpyrrolidone (NEP) still display numerous pinholes even when fabricated at a lower T_A of 16 °C (SI, Fig. S11). These results indicate that clustering based solely on physicochemical descriptors is insufficient for accurately identifying optimal solvents. To enhance prediction accuracy, experimentally validated solvent data were used as labels to train supervised learning classification models (SI, Fig. S12 and S13). Following the training and validation phases, the ensemble model identified the top 20 solvents as promising candidates based on aggregated predictions, with solvent #119 ranking first due to its high probabilities (80.4%), as shown in Fig. 1b. This solvent, 1,3-dimethyl-3,4,5,6-tetrahydro-2(1*H*)-pyrimidinone (DMPU _ #119), was selected for further experimental validation. As shown in Fig. S14 (SI), all DMPU-treated films fabricated at a T_A ranging from 16 to 28 °C exhibit a smooth, dense morphology with excellent coverage, confirming that DMPU effectively broadens the processing T_A window for AFP fabrication. These results also validate the predictive accuracy of the optimized ML model.

To systematically evaluate the impact of ML-selected solvents on broadening the perovskite processing T_A window, the performances of the corresponding photovoltaic devices were characterized. In this study, AFPSCs with the structure of ITO/Me-2PACz/$FAPbI_3$/PCBM/BCP/Ag were fabricated under various T_A conditions. At a T_A of 16 °C, both devices treated with different solvents exhibited comparable performance, with PCEs exceeding 24% (Fig. 1c and Table S1, SI). However, at 28 °C, the PCE of the commonly used NMP-treated AFPSCs dropped significantly from 24.05% to 15.60%, with a large reduction in the fill factor (FF) from 81.20% to 57.72% and the open-circuit voltage (V_{OC}) from 1.16 V to 1.07 V under the reverse current–voltage sweep (Fig. 1d; forward scan data are provided in Fig. S16 and Table S2, SI). The V_{OC} reduction is attributed to increased non-radiative recombination, which is consistent with the above PL mapping results (Fig. S10, SI). Pinholes on the NMP-treated film likely introduced defect states, increasing carrier recombination and lowering V_{OC}. Additionally, these pinholes may have caused direct contact between the electron and hole transport layers, resulting in leakage currents and reduced FF. In contrast, devices treated with DMPU demonstrated improved performance, particularly in FF, due to the reduced number of pinholes in the perovskite films. Notably, DMPU-treated devices showed comparable performance at both 16 °C and 28 °C, indicating a superior temperature tolerance. In addition, as shown in Fig. S17 (SI), the external quantum efficiency (EQE)-integrated current density closely matched with the short-circuit current density (J_{SC}) derived from the *J–V* curves. Regarding the reproducibility of the devices under various T_A values, Fig. 1e shows the statistical results of over 20 NMP-treated and DMPU-treated devices fabricated from 16 °C to 32 °C. It is clearly shown that the PCE of NMP-treated devices dropped significantly while T_A is higher than 20 °C, and became totally failed over 28 °C. The corresponding performance distribution increases from ±7.7% at 24 °C to ±15.2% at 28 °C. On the other hand, DMPU-treated devices demonstrated stable performance when fabricated from 16 °C to 24 °C, with a performance distribution of less than ±2.5%. Even at 28 °C, the performance distribution of DMPU-treated devices is still less than ±4.0%. The superior reproducibility of the performance of DMPU-treated devices directly correlates with their stability and scalability. More importantly, using the same approach with slot-die coating, 30 cm × 30 cm DMPU-treated AFP solar modules demonstrate impressive PCEs of 17.6% with an aperture area of 693 cm^2, indicating their great potential for large-scale production (Fig. 1f and g). It is worth noting that, although the above results demonstrate the effectiveness of ML as a reliable and time-efficient tool for precise solvent selection, selection-algorithm-based ML approaches do not provide mechanistic insight into the origins of the improved performance, in particular: (i) the critical solvent properties influencing AFP film formation, and (ii) their impact on the crystallization process across different T_A values.

Mechanism investigation

As aforementioned, the key to fabricating AFP films lies in mitigating the competition between nucleation and crystal growth. To achieve this, Bu *et al.* employed NMP to form a PbI_2–NMP adduct to prevent PbI_2 from directly reacting with FAI, thus resulting in a retarded crystal growth. This approach enables the formation of dense and uniform films. However, similar to NMP, DMSO has also been demonstrated to interact strongly with PbI_2 to form a stable adduct,[33] but the DMSO-treated films exhibit poor coverage. Therefore, it is questionable if any crucial interacting process during film formation has been overlooked.

Generally, due to the rapid nucleation with the presence of FA cations, FA-based perovskites are often adopted in the development of AFP.[21,23] Therefore, besides PbI_2, we postulated that FA should play a role in the formation of solvent adducts. To explore the interaction between FA cations and solvents, Fourier-transform infrared (FTIR) spectroscopy was performed. It has been reported that FA cations would interact with Lewis base solvents through hydrogen bonding between the amine functional groups of FAI and the Lewis base, strengthening the C═N bond in FAI.[33,34] To analyze this effect, we compared the C═N stretching vibration peak of FAI in DMSO and three other

ML-selected solvents. As shown in Fig. 2a–d, the C═N stretching vibration peak shifts to a higher wavenumber upon interaction with all the solvents. For FAI in DMSO, the C═N peak shows a 10 cm^{-1} shift from 1693 cm^{-1} (bare FAI) to 1700 cm^{-1}. In contrast, the C═N peak shows more than a two-fold shift from 22 cm^{-1} to 27 cm^{-1} in the other three ML-selected solvents, indicating stronger interactions between FAI and NMP, DMI, and DMPU compared to DMSO. Intuitively, the stronger interaction is attributed to the presence of C–N and C═O bonds in the ML-selected solvent molecules, where the lone pair electrons on nitrogen and oxygen atoms serve as hydrogen bond acceptors, promoting stronger hydrogen bonding with FAI, which is supported by the nuclear magnetic resonance (^{1}H NMR) spectra results (Fig. S20, SI).[33] Such an interaction can also be inferred from the appearance of a yellowish mixture (Fig. 2e) after mixing the colorless FAI with colorless NMP, DMI, and DMPU. In comparison, no significant color change is observed when FAI is mixed with DMSO. The presence of the yellowish solvent adducts is further confirmed by the Tyndall effect observed in the three ML-selected solvent/FAI solutions by dynamic light scattering (DLS) measurement (Fig. 2f).[35,36] The average colloidal particle size ($Z_{Average}$) in the DMSO/FAI solution is only 274 nm, whereas the $Z_{Average}$ values in NMP/FAI and DMI/FAI are almost two times larger, and it is even reaching 593 nm in DMPU/FAI. In addition, the increased absorption at ~375 nm in UV-vis spectra of the FAI precursors suggests the presence of more dissociated I^- ions in the solution, indicating stronger interactions between FA and the solvents, as shown in Fig. S21 (SI).

To further evaluate the impact of solvent–FAI interactions on the stability of intermediate adducts, the binding energies of various solvent adducts were calculated using DFT, as shown in Fig. 2g–i. For solvent–PbI_2 adducts, the binding energy of DMSO–PbI_2 (−0.99 eV) is lower than that of NMP and DMI-coordinated adducts (−0.78 eV and −0.77 eV, respectively), which can be attributed to the higher donor number of DMSO.[37,38] This result confirms that DMSO can form a more stable adduct with PbI_2 (SI, Fig. S22). However, the binding

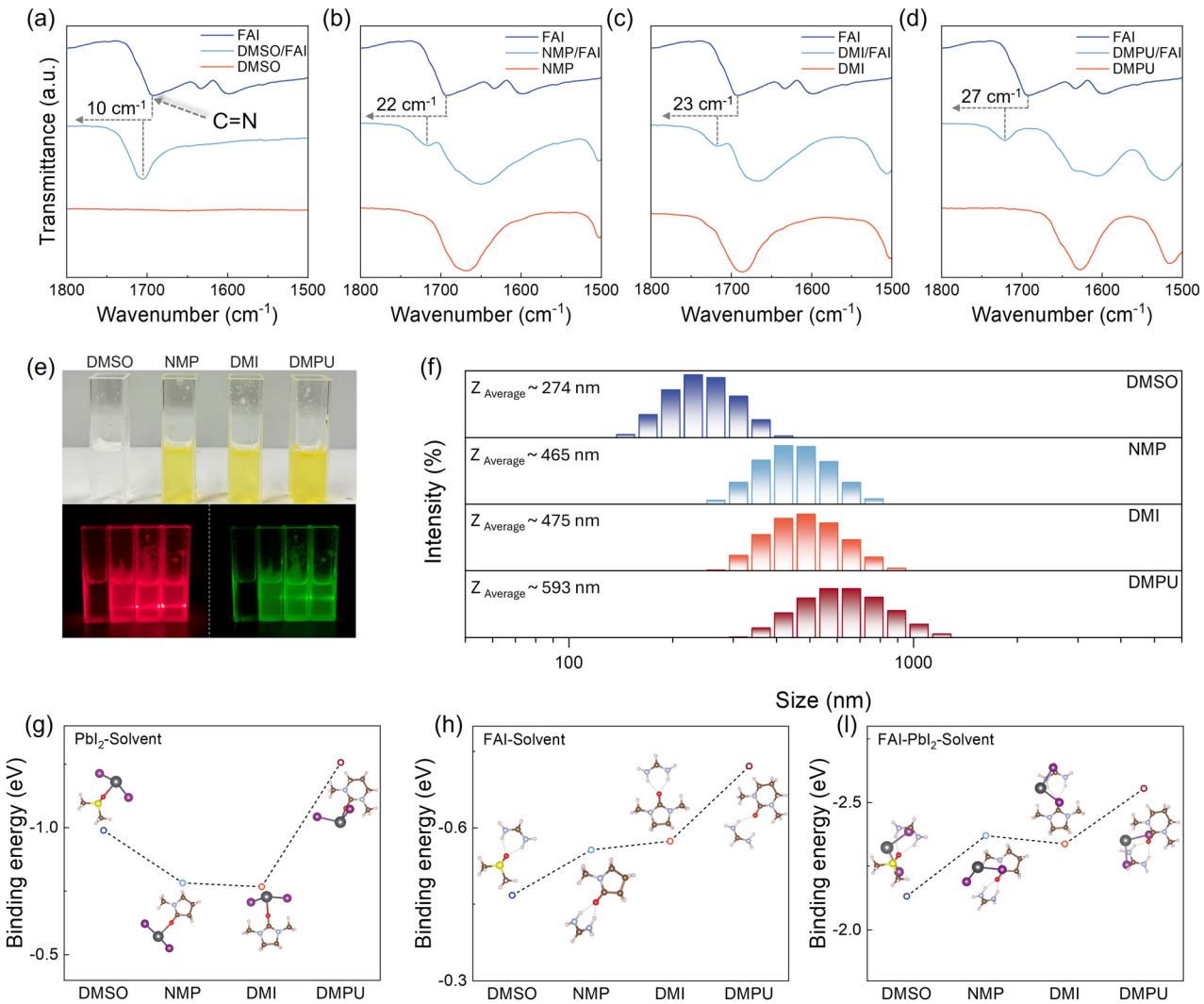

Fig. 2 Interaction between solvents and precursor ions. (a)–(d) FTIR spectra of the bare FAI, FAI/solvents, and bare solvents. (e) Tyndall effect test on the FAI/solvent mixture. (f) DLS result of FAI/solvent mixture. (g)–(i) Binding energies of different solvent-based adducts.

energy between the FA cation and DMSO is only −0.47 eV, significantly higher than that of the other three ML-selected solvents. Similarly, the binding energy of the FAI–PbI_2–DMSO adduct is also higher compared to the adducts formed with the other solvents. Particularly, only the binding energy of the FAI–PbI_2–DMSO adduct is higher than that of $FAPbI_3$ (−2.19 eV), suggesting that DMSO-based adducts exhibit reduced stability in an FA-rich environment. Consequently, the stronger hydrogen bonding interactions between FA and the ML-selected solvents can hinder the interaction between FAI and PbI_2, thereby suppressing the early crystallization and increasing the solvent adduct stability.

The effect of FA on solvent-based adduct formation was further investigated by X-ray diffraction (XRD) measurements on adduct films prepared from precursors with various FA contents, as shown in Fig. 3a and b. In this experiment, NMP, as a prototypical solvent used in AFP, was selected as a representative ML-identified solvent and compared with DMSO. Both DMSO and NMP were used as single solvents (without dimethylformamide (DMF)) to prepare the corresponding solvent-based adducts, with PbI_2 and FAI as solutes. In the case of DMSO, the intensity of the DMSO-based adduct peak (around 10°) decreases as the FA content (FAI/(FAI + PbI_2) ratio) increases from 0% to 100%.[39] Simultaneously, the intensity of the PbI_2 peak (12.9°) gradually increases with higher FA content.[40] Notably, when the molar ratio of FAI in the precursor reaches 100%, no solvent adduct phase is detected, and only the PbI_2 peak is observed. Combined with the previously discussed binding energy results, the FA cation appears to disrupt the DMSO–PbI_2 adduct structure, thereby facilitating the formation of $FAPbI_3$. However, $FAPbI_3$ is unstable in humid air and readily degrades back to PbI_2, which explains the

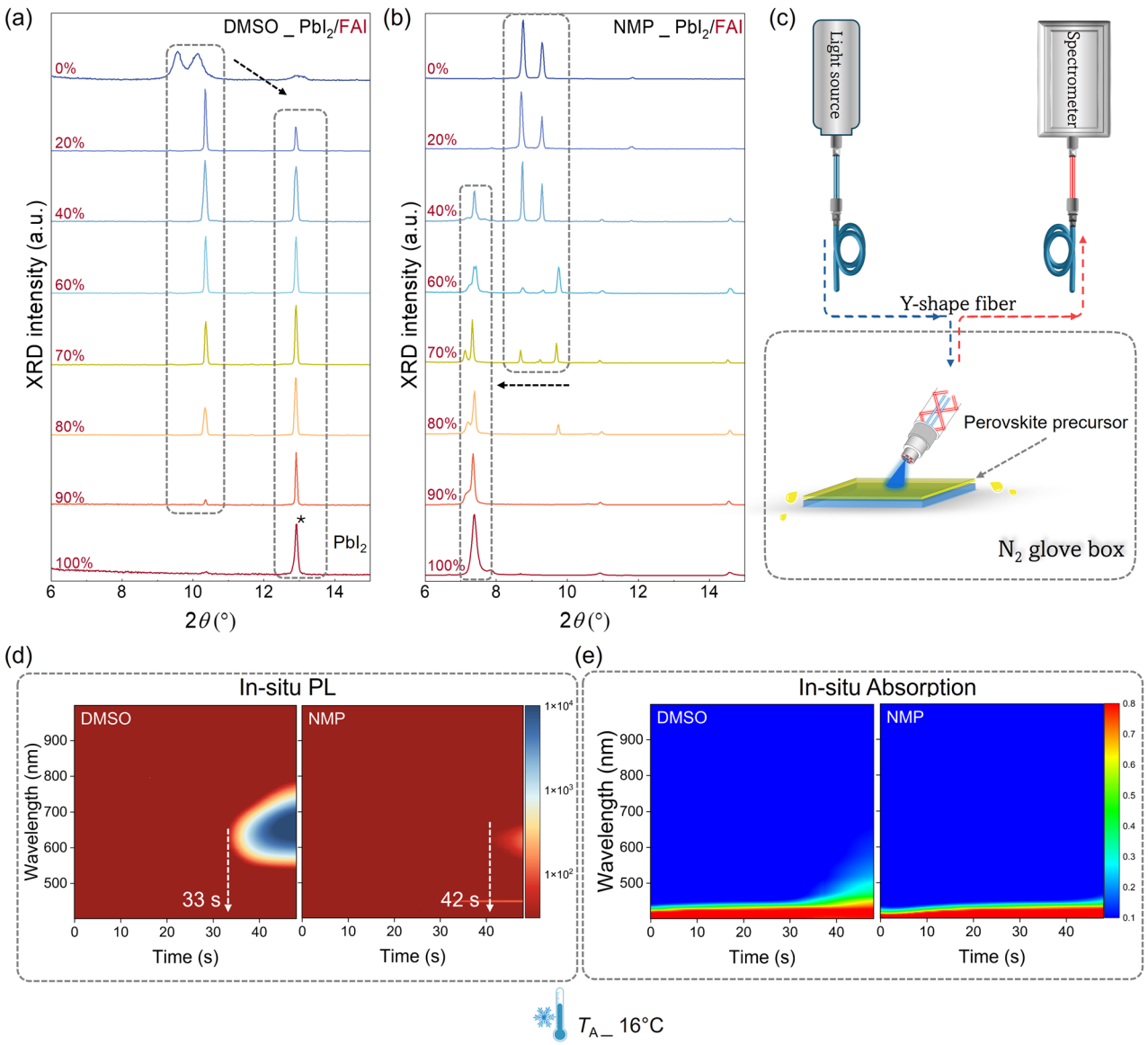

Fig. 3 Crystallization process of solvent-treated AFP. (a) and (b) XRD spectra of different solvent-based adducts with various FA contents. (c) Schematic drawing of *in situ* optical tests. *In situ* (d) PL and (e) absorption results of different solvent-treated films fabricated at a T_A of 16 °C during spin-coating.

observed precipitation of PbI_2 during XRD testing. In contrast, the NMP–PbI_2 adduct remains stable after adding 20% FA. With further increases in FA content, a new peak at 7° appears, corresponding to the gradual formation of the NMP–PbI_2–FAI adduct.[20,21] Notably, no PbI_2 or δ-phase is detected, highlighting the superior stability of the NMP-based adduct even in an FA-rich environment. Time-resolved XRD measurements further confirm that the solvent adducts are the primary product formed during the spin-coating (Fig. S23, SI), and the phase conversion can only be observed in the DMSO–PbI_2 adduct, while the NMP–PbI_2–FAI adduct is relatively stable.

We sought to investigate perovskite nucleation and crystal growth dynamics with different solvents and examine their corresponding effects under varying ambient temperatures through an *in situ* optical probing method. Fig. 3c illustrates the custom-built *in situ* optical setup for PL and absorption measurements, housed within a temperature-controlled and nitrogen-filled glovebox (detailed information is given in Methods of supplementary information). Fig. 3d presents 2D contour plots of *in situ* PL results recorded during spin-coating at 16 °C, where "0 s" on the *x*-axis marks the onset of spin-coating. For the DMSO-treated sample, gradual solvent evaporation leads to an increase in solute concentration, initiating nucleation at 33 s. A noticeable PL signal was detected at this point, followed by a rapid increase in PL intensity over the next 20 s, indicating the formation of a large number of luminous nuclei—a hallmark of fast nucleation (detailed intensity and peak position changes are given in Fig. S24, SI).[25,41,42] Concurrently, the PL peak shifted from 600 nm to 700 nm, which is attributed to grain growth reducing the quantum confinement effect.[43–45] These observations suggest that the DMSO-treated film undergoes rapid nucleation and crystal growth simultaneously, with competition between these processes potentially causing pinhole formation. In contrast, the onset of the PL signal in the NMP-treated sample was delayed until 42 s. The slower rise in PL intensity indicates fewer luminous nuclei and thus slower nucleation, it is attributed to the strong bonding between NMP and FA cations, as noted earlier. In addition, in the NMP-treated sample, the constant PL peak wavelength at 620 nm throughout the process suggests retarded growth of the formed nuclei. Consistently, the *in situ* absorption results (Fig. 3e and Fig. S25, SI) also revealed crystal growth in the DMSO-treated sample, whereas the NMP-treated film also showed absorption from intermediate adducts.[46] For the DMSO-treated sample, the absorption edge continuously red-shifts toward longer wavelengths, reaching approximately 600 nm. In contrast, the absorption edge of the NMP-treated film remains within the characteristic range of the solvent-based adduct phase (400–450 nm), indicating the persistence of the intermediate adduct phase throughout the entire spin-coating process. As shown in Fig. S26 (SI), compared to NMP, no obvious perovskite nucleation was observed in samples using DMI and DMPU as solvents. This observation is consistent with the computational results, which indicate the formation of strong solvent-based adducts.

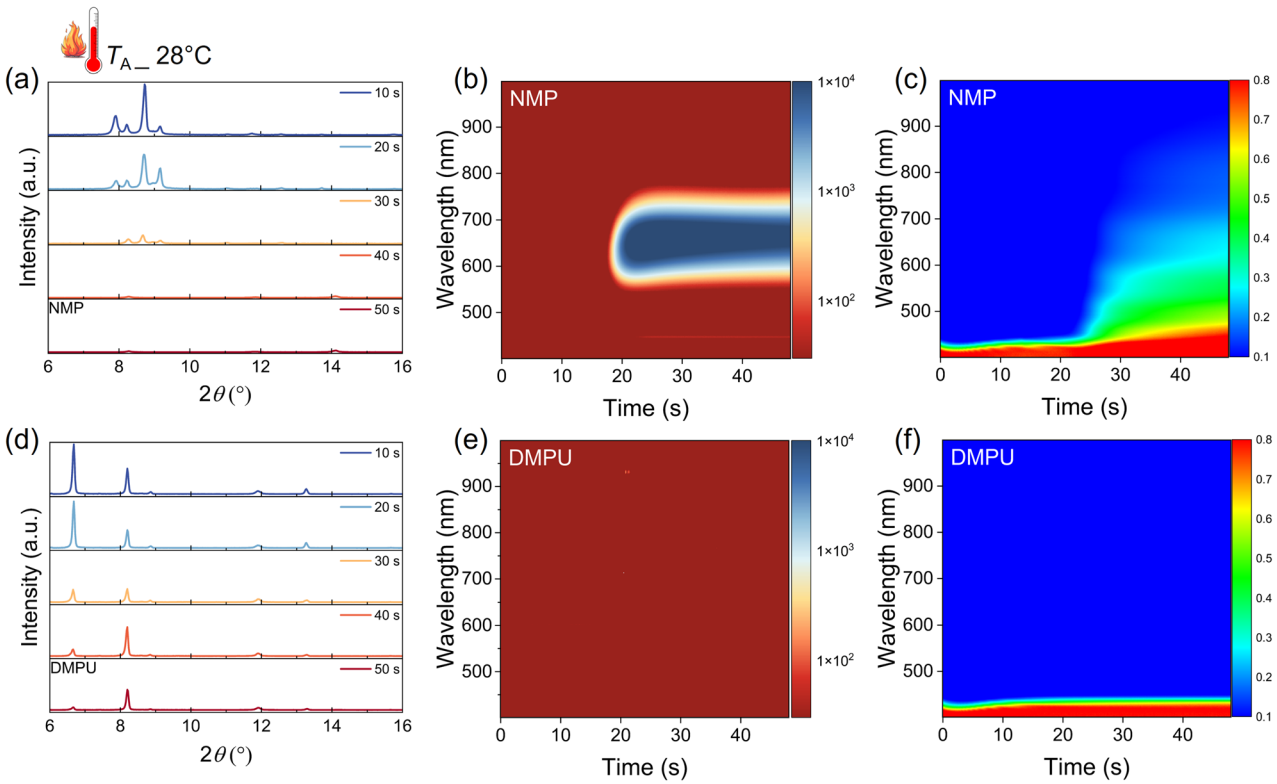

Fig. 4 Crystallization process regulated by DMPU at a higher T_A. Time-resolved XRD spectra of AFP films treated by (a) NMP and (d) DMPU during spin-coating. *In situ* (b) and (e) PL and (c) and (f) absorption results of different solvent-treated films during spin-coating. The T_A is 28 °C.

More importantly, such stable adduct formation is believed to be critical for expanding the T_A processing window. Indeed, an examination of the crystalline structure of the DMPU-treated film, as shown in Fig. S27 (SI), shows that the DMPU-based adduct exhibits greater thermal stability. Such a stable intermediate will strongly affect the crystallization process. As shown in Fig. 4a and d, the time-resolved XRD spectra indicate that the NMP-based adduct signal decreases dramatically after spin-coating for 30 s at a T_A of 28 °C. In contrast, strong adduct diffraction is detected in the whole spin-coating process in the DMPU-treated film, indicating better stability. This is consistent with the previous DFT results, where DMPU has stronger binding to the precursor ions. The effect of stable intermediates on the crystallization is further investigated by *in situ* optical measurements. As shown in Fig. 4b, when the T_A is increased to 28 °C, the PL signal in the NMP-treated film appears earlier than in the film fabricated at 16 °C (at 18 s and 42 s, respectively). Furthermore, the PL intensity increases more rapidly, accompanied by a noticeable redshift in the peak position (detailed intensity and peak position changes are given in Fig. S28, SI). This suggests a fast crystallization process in the NMP-treated film at higher temperatures, leading to the formation of pinholes on the film surface. In contrast, no detectable PL signal is observed during spin-coating of the DMPU-treated film at 28 °C, indicating retarded perovskite nucleation (Fig. 4e). This is comparable to the performance of the NMP-treated film at a lower temperature. The delayed nucleation is attributed to the strong interaction between DMPU and FA cations, which suppresses the reaction between FAI and PbI_2 to form perovskite nuclei. As a result, the DMPU-treated AFP film fabricated at 28 °C still forms a dense, pinhole-free surface. Consistently, no sign of crystallization can be observed in the

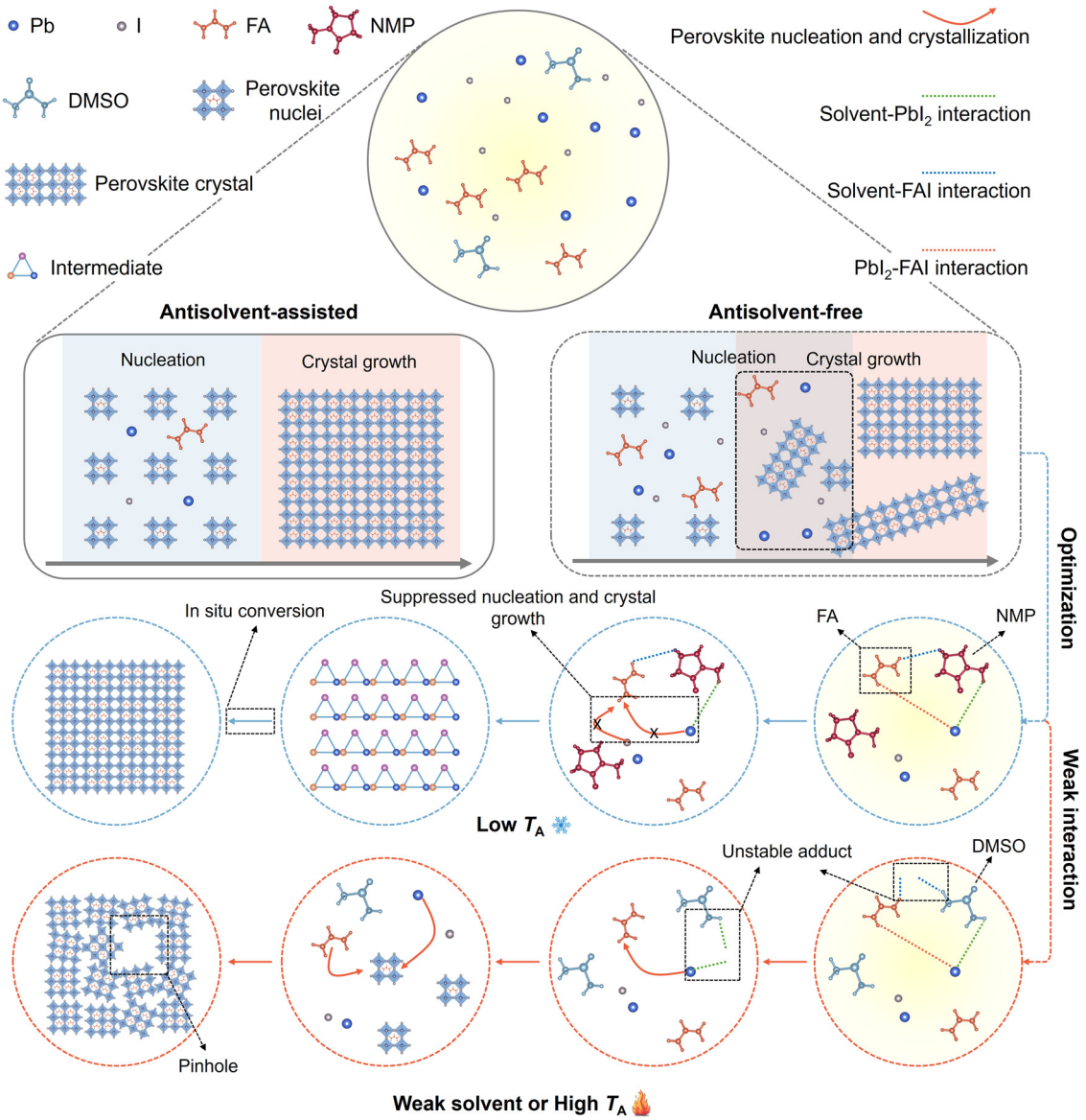

Fig. 5 Schematic diagram of possible phase evolution in the crystallization of solution-processed perovskites.

DMPU-treated film in the *in situ* absorption results, in sharp contrast to the NMP-treated films (Fig. 4c and f). Notably, due to the strong binding affinity of DMPU, high concentration of DMPU will lead to a perovskite film with poor morphology, as shown in Fig. S29 (SI). Therefore, a mixed DMPU:NMP is necessary to optimize the film morphology. On the other hand, an interesting phenomenon during spin-coating was observed: no PL or absorption signals in high-quality AFP films emerged, regardless of low or high T_A (Fig. 3d, e and 4e, f), indicating the absence of perovskite nuclei formation. This observation challenges the long-standing belief that rapid nucleation is essential for achieving high-quality films by ensuring uniform nuclei distribution and controlled grain growth.[47,48] However, in the AFP system, rapid nucleation is inherently challenging and often uncontrollable. Instead, the formation of an intermediate phase emerges as a viable alternative, facilitating a uniform distribution of precursor ions and circumventing the limitations of rapid nucleation.

Overall, nucleation and crystal growth are critical factors that determine the quality of perovskite thin films in solution-processed fabrication. According to the above results, the differences in crystallization dynamics between antisolvent-assisted perovskite and AFP fabrication processes are illustrated in Fig. 5. In antisolvent-assisted fabrication, the rapid extraction of the antisolvent promotes fast and complete nucleation, ensuring a uniform distribution of perovskite nuclei and precursor ions before crystal growth, resulting in dense perovskite films. However, the crystallization rate will be further increased at a higher T_A, which may lead to the nuclei collision and aggregation, finally resulting in the inhomogeneous growth (cracks) due to solute depletion. In contrast, AFP fabrication generally exhibits a slower nucleation rate. In this process, unconsumed precursor ions are simultaneously used for nucleation and diffusion toward existing nuclei, which suppresses further nucleation and promotes crystal growth, inhibiting the uniform distribution of nuclei and ions. This leads to poor film coverage and the formation of pinholes. To address this issue, solvent engineering strategies have been employed to enable uniform precursor ion distribution by forming solvent–PbI_2 adducts in the as-deposited film prior to crystal growth during thermal annealing. However, previous studies have primarily focused on the impact of solvent adducts on AFP fabrication while overlooking their formation mechanism. This oversight has led to the unexpected observation that DMSO, a commonly used solvent additive in other solution-processed methods, is unsuitable for AFP fabrication, a phenomenon that remains poorly understood. Here, we found that the interaction between FA and the solvent plays a crucial role in solvent adduct formation. FA disrupts the solvent–PbI_2 adduct by interacting with PbI_2, whereas solvents containing nitrogen and oxygen atoms can form hydrogen bonds with FA cations (also may be related to the rotatable bond count, as shown in Fig. S30, SI). These bonds effectively prevent the reaction between PbI_2 and FAI, stabilizing the solvent adduct and slowing perovskite crystallization. Importantly, if the interaction between FA and the solvent (*e.g.*, DMSO) is insufficiently strong, the solvent adduct cannot be maintained under FA-rich conditions, resulting in poor film morphology. Additionally, this interaction between FA and the solvent can be disrupted at a higher T_A, which limits the processing T_A of AFPSCs to below 18 °C. Therefore, selecting a solvent capable of strongly interacting with FA cations to form a stable solvent adduct under FA-rich conditions is critical for achieving high-quality films and expanding the processing T_A window in AFP fabrication.

Conclusion

We demonstrate an ML-guided strategy for identifying solvent additives to widen the T_A processing window for FA-based AFP fabrication. Using this approach, high-efficiency AFPSCs with PCE exceeding 24% are achieved over a broad T_A range from 16 °C to room temperature (24 °C). Mechanistically, we demonstrate that achieving a uniform distribution of precursor ions prior to crystal growth is a critical requirement for forming high-quality AFP films, thereby challenging the prevailing emphasis on rapid and complete perovskite nucleation. This uniform ion distribution arises from the simultaneous formation of stable solvent adducts with both precursor anions and cations. Consequently, in addition to the strong solvent–PbI_2 coordination alone, our findings reveal that forming stable adducts between the solvent and FA^+ is essential to suppress the nucleation. Overall, this study presents a systematic ML-guided strategy for solvent selection and provides new insights into the role of perovskite intermediates in governing crystallization pathways, offering practical guidance for the scalable fabrication of high-performance AFP thin films.

Author contributions

Y. W., W. Z., and Z. Z. conceived and designed the research. Y. W., Z. Y., and Z. Z. performed *in situ* measurements and data analysis. Z. Z., J. W., and H. L. carried out the device fabrication. J. W. and H. D. carried out the device characterization studies. W. Z. performed machine learning analysis. Y. Z. conducted the DFT calculation. Y. J. and J. Z. carried out film characterization. Y. C., J. H., T. W., and H. L. Y. helped to optimize the perovskite solar cells. Y. W. and W. Z. wrote the first draft of the paper. Z. Z., Y. C., D. Z., and S. W. T. supervised the project and contributed to the manuscript draft. All co-authors discussed the results and commented on the paper.

Conflicts of interest

The authors declare no conflicts of interest.

Data availability

The data supporting this article have been included as part of the supplementary information (SI), which includes experimental methods, machine learning details, 31 figures, and 2 tables. See DOI: https://doi.org/10.1039/d6ee00170j.

Acknowledgements

We acknowledge the General Research Fund (CityU 11304420 and CityU 11317422) from the Research Grants Council of Hong Kong SAR, China.

References

1 A. Kojima, K. Teshima, Y. Shirai and T. Miyasaka, *J. Am. Chem. Soc.*, 2009, **131**, 6050–6051.
2 N. J. Jeon, J. H. Noh, Y. C. Kim, W. S. Yang, S. Ryu and S. I. Seok, *Nat. Mater.*, 2014, **13**, 897–903.
3 H. S. Jung and N. G. Park, *Small*, 2015, **11**, 10–25.
4 H. Chen, C. Liu, J. Xu, A. Maxwell, W. Zhou, Y. Yang, Q. Zhou, A. S. Bati, H. Wan and Z. Wang, *Science*, 2024, **384**, 189–193.
5 M. A. Green, E. D. Dunlop, M. Yoshita, N. Kopidakis, K. Bothe, G. Siefer, D. Hinken, M. Rauer, J. Hohl-Ebinger and X. Hao, *Prog. Photovoltaics*, 2024, **32**, 425–441.
6 Y. Wang, P. Xiang, A. Ren, H. Lai, Z. Zhang, Z. Xuan, Z. Wan, J. Zhang, X. Hao and L. Wu, *ACS Appl. Mater. Interfaces*, 2020, **12**, 53973–53983.
7 M. Jung, S.-G. Ji, G. Kim and S. I. Seok, *Chem. Soc. Rev.*, 2019, **48**, 2011–2038.
8 J.-W. Lee, S. Tan, S. I. Seok, Y. Yang and N.-G. Park, *Science*, 2022, **375**, eabj1186.
9 Z. Li, T. R. Klein, D. H. Kim, M. Yang, J. J. Berry, M. F. Van Hest and K. Zhu, *Nat. Rev. Mater.*, 2018, **3**, 1–20.
10 National Renewable Energy Laboratory. (2025 February 13). Best Research-Cell Efficiency Chart. https://www2.nrel.gov/pv/cell-efficiency, (accessed 08 16, 2023).
11 Z. Zhang, Y. Wang, W. Wang, Y. Huang, S. Ouyang, Y. Sun, F. Wang, X. Zhou, G. Xing and S. K. So, *Adv. Mater.*, 2026, e19793.
12 J. Prakash, A. Singh, G. Sathiyan, R. Ranjan, A. Singh, A. Garg and R. K. Gupta, *Mater. Today Energy*, 2018, **9**, 440–486.
13 L. Yan, H. Huang, P. Cui, S. Du, Z. Lan, Y. Yang, S. Qu, X. Wang, Q. Zhang and B. Liu, *Nat. Energy*, 2023, **8**, 1158–1167.
14 M. Yang, Z. Li, M. O. Reese, O. G. Reid, D. H. Kim, S. Siol, T. R. Klein, Y. Yan, J. J. Berry and M. F. Van Hest, *Nat. Energy*, 2017, **2**, 1–9.
15 H.-H. Huang, Q.-H. Liu, H. Tsai, S. Shrestha, L.-Y. Su, P.-T. Chen, Y.-T. Chen, T.-A. Yang, H. Lu and C.-H. Chuang, *Joule*, 2021, **5**, 958–974.
16 C. Liu, Y.-B. Cheng and Z. Ge, *Chem. Soc. Rev.*, 2020, **49**, 1653–1687.
17 L. Chao, T. Niu, W. Gao, C. Ran, L. Song, Y. Chen and W. Huang, *Adv. Mater.*, 2021, **33**, 2005410.
18 Z. Saki, M. M. Byranvand, N. Taghavinia, M. Kedia and M. Saliba, *Energy Environ. Sci.*, 2021, **14**, 5690–5722.
19 A. Ng, Z. Ren, H. Hu, P. W. Fong, Q. Shen, S. H. Cheung, P. Qin, J. W. Lee, A. B. Djurišić and S. K. So, *Adv. Mater.*, 2018, **30**, 1804402.
20 T. Bu, J. Li, H. Li, C. Tian, J. Su, G. Tong, L. K. Ono, C. Wang, Z. Lin and N. Chai, *Science*, 2021, **372**, 1327–1332.
21 T. Bu, L. K. Ono, J. Li, J. Su, G. Tong, W. Zhang, Y. Liu, J. Zhang, J. Chang and S. Kazaoui, *Nat. Energy*, 2022, **7**, 528–536.
22 Q. Zhang, G. Ma, K. A. Green, K. Gollinger, J. Moore, T. Demeritte, P. C. Ray, G. A. Hill Jr, X. Gu and S. E. Morgan, *ACS Appl. Energy Mater.*, 2022, **5**, 1487–1495.
23 D. Wang, J. Chen, P. Zhu, Y. Qiao, H. Hu, J. Zeng, J. Zhang, G. Qu, Y. Wang and X. Wang, *Adv. Energy Mater.*, 2023, **13**, 2203649.
24 J. Li, C. Jin, R. Jiang, J. Su, T. Tian, C. Yin, J. Meng, Z. Kou, S. Bai and P. Müller-Buschbaum, *Nat. Energy*, 2024, 1–11.
25 Y. Wang, Z. Zeng, Y. Zhang, Z. Zhang, L. Bi, A. He, Y. Cheng, A. K. Y. Jen, J. C. Ho and S. W. Tsang, *Adv. Mater.*, 2024, **36**, 2307635.
26 Y. Wang, Z. Zhang, Z. Zeng, Y. Zhang, T. Hu, L. Bi, Y. Yang, S. Ouyang, X. Hao and C. Xu, *ACS Energy Lett.*, 2025, **10**, 647–657.
27 N. Li, X. Niu, L. Li, H. Wang, Z. Huang, Y. Zhang, Y. Chen, X. Zhang, C. Zhu and H. Zai, *Science*, 2021, **373**, 561–567.
28 M. Saliba, J.-P. Correa-Baena, C. M. Wolff, M. Stolterfoht, N. Phung, S. Albrecht, D. Neher and A. Abate, *Chem. Mater.*, 2018, **30**, 4193–4201.
29 B. Jo, W. Chen and H. S. Jung, *J. Energy Chem.*, 2025, **101**, 298–323.
30 Q. Zhang, H. Wang, Q. Zhao, A. Ullah, X. Zhong, Y. Wei, C. Zhang, R. Xu, S. De Wolf and K. Wang, *ACS Energy Lett.*, 2024, **9**, 5924–5934.
31 C. Zhi, S. Wang, S. Sun, C. Li, Z. Li, Z. Wan, H. Wang, Z. Li and Z. Liu, *ACS Energy Lett.*, 2023, **8**, 1424–1433.
32 J. Wu, L. Torresi, M. Hu, P. Reiser, J. Zhang, J. S. Rocha-Ortiz, L. Wang, Z. Xie, K. Zhang and B.-W. Park, *Science*, 2024, **386**, 1256–1264.
33 J.-W. Lee, Z. Dai, C. Lee, H. M. Lee, T.-H. Han, N. De Marco, O. Lin, C. S. Choi, B. Dunn and J. Koh, *J. Am. Chem. Soc.*, 2018, **140**, 6317–6324.
34 M. Li, R. Sun, J. Chang, J. Dong, Q. Tian, H. Wang, Z. Li, P. Yang, H. Shi and C. Yang, *Nat. Commun.*, 2023, **14**, 573.
35 X. Yu, Z. Fang, S. Lin, S. Wu, M. Fang, H. Xie, D. Kong and C. Zhou, *Small*, 2024, **20**, 2306101.
36 X. Zhao, R. Luo, C. Yu, X. Xu, W. Zhu, Y. Min and N. Cai, *Adv. Funct. Mater.*, 2024, **34**, 2307568.
37 Y. Zou, W. Yu, H. Guo, Q. Li, X. Li, L. Li, Y. Liu, H. Wang, Z. Tang and S. Yang, *Science*, 2024, **385**, 161–167.
38 J. C. Hamill Jr, J. Schwartz and Y.-L. Loo, *ACS Energy Lett.*, 2017, **3**, 92–97.
39 M. Lu, C. Shi, C. Ma, N. Li, L. Li and G. Xiao, *J. Mater. Sci.: Mater. Electron.*, 2017, **28**, 5603–5608.
40 A. Alberti, C. Bongiorno, E. Smecca, I. Deretzis, A. La Magna and C. Spinella, *Nat. Commun.*, 2019, **10**, 2196.
41 A. He, Y. Wang, P. Tang, Z. Zhang, Z. Zeng, Y. Zhang, X. Hao, L. Wu, S. K. So and S. W. Tsang, *Adv. Energy Mater.*, 2023, **13**, 2300957.

42 L. Bi, Q. Fu, Z. Zeng, Y. Wang, F. R. Lin, Y. Cheng, H.-L. Yip, S. W. Tsang and A. K.-Y. Jen, *J. Am. Chem. Soc.*, 2023, **145**, 5920–5929.
43 V. D'Innocenzo, A. R. Srimath Kandada, M. De Bastiani, M. Gandini and A. Petrozza, *J. Am. Chem. Soc.*, 2014, **136**, 17730–17733.
44 M. Shirayama, H. Kadowaki, T. Miyadera, T. Sugita, M. Tamakoshi, M. Kato, T. Fujiseki, D. Murata, S. Hara and T. N. Murakami, *Phys. Rev. Appl.*, 2016, **5**, 014012.
45 Z. Zeng, Y. Wang, S. Ding, Y. Li, C. Xiang, C. S. Lee, Y. Cheng and S. W. Tsang, *Adv. Funct. Mater.*, 2024, 2404255.
46 L. Yin, W. Huang, J. Fang, Z. Ding, C. Jin, Y. Du, L. Lang, T. Yang, S. Wang and W. Cai, *Adv. Mater.*, 2023, **35**, 2303384.
47 D. Bi, C. Yi, J. Luo, J.-D. Décoppet, F. Zhang, S. M. Zakeeruddin, X. Li, A. Hagfeldt and M. Grätzel, *Nat. Energy*, 2016, **1**, 1–5.
48 K. L. Wang, Z. H. Su, Y. H. Lou, Q. Lv, J. Chen, Y. R. Shi, C. H. Chen, Y. H. Zhou, X. Y. Gao and Z. K. Wang, *Adv. Energy Mater.*, 2022, **12**, 2201274.

